

Chiral three-dimensional isotropic lattices with negative Poisson's ratio

Chan Soo Ha, Michael E. Plesha, Roderic S. Lakes*

August 9, 2016

Department of Engineering Physics, University of Wisconsin, Madison, WI 53706-1687, USA

Keywords (isotropy, chirality, negative Poisson's ratio, auxetic, Cosserat)

* Corresponding author. email lakes@engr.wisc.edu Phone: +00 608 265 8697

Abstract

Chiral three-dimensional isotropic cubic lattices with rigid cubical nodules and multiple deformable ribs are developed and analyzed via finite element analysis. The lattices exhibit geometry dependent Poisson's ratio that can be tuned to negative values. Poisson's ratio decreases from positive to negative values as the number of cells increases. Isotropy is obtained by adjustment of aspect ratio. The lattices exhibit significant size effects. Such a phenomenon cannot occur in a classical elastic continuum but it can occur in a Cosserat solid.

Preprint adapted from Ha, C. S., Plesha, M. E., Lakes, R. S., "Chiral three-dimensional isotropic lattices with negative Poisson's ratio", *Physica Status Solidi B*, 253, (7), 1243-1251 (2016).

1 Introduction

Chiral materials and structures do not have a center of symmetry. There is a distinction between right and left so they are not invariant to inversion of coordinates. Quartz is a crystal that is chiral at the inter-atomic level [1]. There is left and right quartz. Chirality may also be designed in composites on various length scales. A planar chiral lattice with Poisson's ratio -1 [2] was developed. The cell size was several centimeters. Poisson's ratio was -1, essentially independent of strain, via experiment and analysis. In contrast, negative Poisson's ratio of (3D) foams [3] and of (2D) honeycombs [4] with inverted hexagonal cells of bow-tie shape depends on strain. 2D structures with rotating hexamers and trimers [5] can exhibit negative Poisson's ratio of large magnitude. Negative Poisson's ratio materials have been called "anti-rubber" [6] or "auxetic" [7] [8].

Chiral 2D lattices have been analyzed for use as structural honeycomb [9] [10] that may be used in sandwich panels for airplane wings that morph or change shape. Buckling [11] [12] deformation of lattices of this type has been studied in a structural context. Lattices have been made with sensors and actuators [13]. These are referred to as smart structures. The lattices exhibit tunable band gaps [14] in wave propagation; potentially useful in reducing vibration.

Three dimensional lattices provide design freedom in contrast with foams [15], the structure of which is a consequence of the foaming method. 3D lattices with triangulated cells are stiffer than foams made of the same rib material. The reason is the ribs in the triangulated structure deform axially rather than in bending [16] as they do in foams. A negative Poisson's ratio 3D model was

developed [17] in order to elucidate the deformation mechanisms of α -cristobalite [18], a negative Poisson’s ratio form of silicon dioxide. A 3D structure containing corner-linked cubical nodules was developed [19] to model structure property relations of an auxetic microporous polymer [20]. 3D lattices with a negative Poisson’s ratio [21] have been designed and fabricated.

Continuum mechanics is used when the size of an object is sufficiently larger than the size of its microstructure. In most analyses of cellular solids (e.g. [15]), the continuum is classical. Classical elasticity has no length scale. If the cell size is not small compared with length scales associated with the object or with strain gradients imposed on it, then it is sensible to use a more general continuum model. Cosserat (micropolar) elasticity [22] is a continuum elasticity theory which contains a length scale. Chiral 2D lattices [2] have been analyzed [23] [24] in the context of Cosserat elasticity.

In the present research, 3D chiral lattices [25] with cubic structure are designed to be elastically isotropic. The rationale of having isotropy is that it provides a simpler interpretation. Also, any novel or unusual effects in an elastically isotropic solid cannot be ascribed to directional anisotropy. Size effects are studied and interpreted via Cosserat elasticity.

2 Analysis

Lattice structures were designed using the same finite element analysis (FEA) approach as we have done previously [25], using the FEA program ANSYS (release 14.5). Here the ribs are made thicker than in [25] and the aspect ratio is tuned to obtain elastic isotropy. Lattices were designed based on the unit cell (1x1x1) shown in figure 1a. This cell was constructed using eight essentially rigid cubes at the corners of the cell (with cube side length a) and numerous deformable ribs (i.e., beams) connecting different corners of cubes to one another as shown. Note that chirality is introduced here. The center-to-center cube spacing is L , and aspect ratio of the unit cell is defined as L/a , which is always greater than unity. The ribs are made of steel with Young’s modulus $E = 200$ GPa and Poisson’s ratio $\nu = 0.3$, and have circular cross section with diameter of the ribs equal to $200 \mu\text{m}$. The ratio of the cube side length to the rib diameter, a/d is then equal to 5. In prior analysis [25], this ratio was equal to 100. While such a ratio reveals behavior of stretch-dominated lattices, thicker ribs are pertinent to bend dominated structures and to the possibility of manufacture via 3D printing. A three dimensional isotropic chiral lattice was fabricated by fused deposition modeling (FDM) technology is shown in figure 2. A Dimension Elite 3D printer with Stratasys ABSplus P430 thermoplastic was used here; the finest resolution is 0.178 mm. A prototype was first designed and was represented by SolidWorks 2015 in .stl (StereoLithography) format. Additional support materials (P400 SR) were removed by dissolving them in detergent and water.

A finite element model for the unit cell was constructed as described in [25]. Each rib was modeled using one beam finite element and each cube was modeled using 24 shell finite elements. The beam finite element includes shear deformation (i.e., they are based on Timoshenko beam theory). Nonetheless, despite the relatively low aspect ratio of the beams, ℓ_{rib}/d , in our model (e.g., for a lattice with L/a equal to 2, ℓ_{rib}/d is 7.07), shear deformations are not expected to be a significant source of deformation; they are dominated by bending and torsion. The elastic modulus for the shell elements was taken to be eight orders of magnitude greater than E of the ribs, so that effectively the cubes are rigid. As such, each cube is a hollow object where its six surfaces are discretized using four shell elements each. The merit of this treatment is that all nodes throughout the finite element model have the same degrees of freedom, namely three translations and three rotations, which makes it straightforward to connect the ribs to the cubes. Furthermore, by using

four shell elements for each surface of a cube, there is a node present in the center of each cube's face, which is convenient for purposes of applying loads and supports. Using this unit cell, lattices of multiple unit cells were constructed as shown in figure 1b, and various aspect ratios including 1.5, 1.8, 2, 2.2, 5, 10 and 20 were modeled.

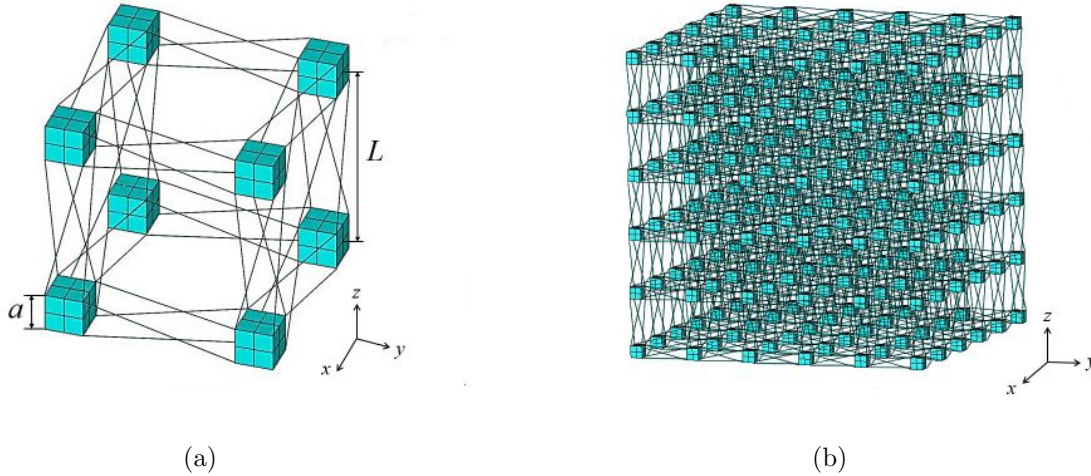


Figure 1: (a) Unit cell of chiral lattice structure (1x1x1). (b) A structure with five cells per side (5x5x5). The aspect ratio is defined to be L/a , where $L/a > 1$. Note that the cubes and ribs shown here are not to scale; ribs are shown as lines for providing a better view of chirality.

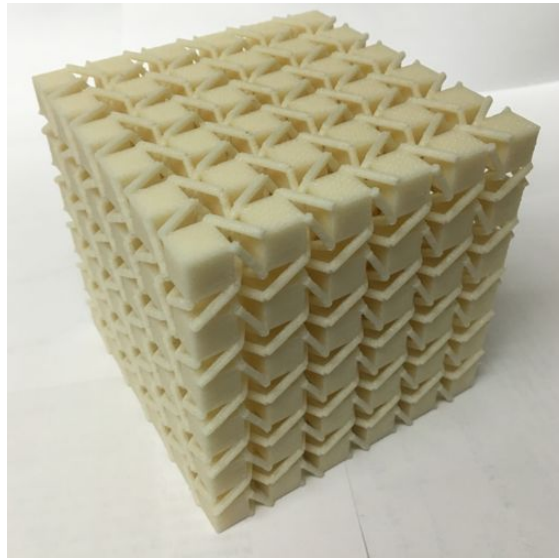


Figure 2: A photograph of a 3d-printed 5x5x5 lattice with an aspect ratio of 1.642. The lattice is about 92 mm on a side.

To determine an effective Young's modulus of the lattices in response to axial compression loading, equal point loads in the negative z direction were applied to the center node of each cube on the upper surface of the lattice (the surface with positive z as the normal direction) as shown in figure 3a for the 2x2x2 lattice. Support conditions on the opposite surface of the lattice (the surface with negative z as the normal direction) consisted of zero z direction translation for all center nodes

on cubes. To prohibit rigid body motion of the lattice, this surface also has the x displacement at one node and the y displacement at one node constrained, plus one more constraint to prevent rotation about the z direction. Thus, the bottom surface of the lattice is supported by rollers and the Poisson effect is allowed to fully develop. Note that there are other ways of applying uniform compression loading to the top surface of our finite element models. We have chosen to apply forces to nodes on the top surface, whereas another option is to prescribe z direction displacements. The disadvantage with the latter case is that it will not allow warping displacements in the z direction to develop, which we observe do occur due to the chirality of our model. Hence, among these two basic choices for applying loading (i.e., prescribed forces versus prescribed displacements) we believe using prescribed forces is more accurate for our purposes.

Elastic isotropy was achieved by tuning the aspect ratio such that the elastic relation $E/2G(1 + \nu) = 1$ between Young's modulus E , shear modulus G , and Poisson's ratio ν is obtained. To that end, pure shear loadings were applied to the lattices in order to determine an effective shear modulus. To model pure shear, equal point loads were applied to the center node of each cube on the appropriate surfaces of the lattice (the surfaces parallel to the xy and xz planes), as shown in figure 3b. The surface whose normal is the negative z direction was constrained to eliminate rigid body motion of the lattice; namely, as shown in figure 3b, the x , y and z displacements at one node, and y and z displacements at another node, and z displacement at yet another node are constrained. For the present chiral lattices, E and ν were obtained from a compression simulation and G from a pure shear simulation. The quantity $E/2G(1 + \nu)$ was used as a measure of isotropy; this was computed for all lattice structures, except $1 \times 1 \times 1$ lattices, and for all aspect ratios. The results for the $1 \times 1 \times 1$ lattices were not used in this process because models with only one cell are better viewed as structures. Aspect ratios resulting in elastic isotropy were determined by fitting computed measures of isotropy (seven data points for each lattice structure) to a 5th degree polynomial using a least-squares best fit. Indeed, a lower degree polynomial best fit would probably be sufficient, but the merit to a 5th degree polynomial is that it is able to fit the number of data points we have (seven) better.

Finite element simulations were performed for all lattice structures ($1 \times 1 \times 1$ through $6 \times 6 \times 6$), and for seven aspect ratios for each of these. The displacements and rotations of all nodes in the lattices were computed in each finite element simulation. Effective strains throughout each unit cell in the lattices were computed similar to our previous research [25] by using the polynomial interpolation

$$u_x = a_1 + a_2x + a_3y + a_4z + a_5xy + a_6yz + a_7xz + a_8xyz \quad (1)$$

The coefficients a_1 through a_8 were determined by fitting this polynomial to the eight x direction displacements for each cube in one unit cell of the lattice. Likewise, this process was repeated for determining polynomials for the y and z direction displacements, namely u_y and u_z . Equation 1 allows the average continuum strains throughout each unit cell to be determined by using the standard definition of small strains

$$\epsilon_{ij} = \frac{1}{2} \left(\frac{\partial u_i}{\partial x_j} + \frac{\partial u_j}{\partial x_i} \right) \quad (2)$$

where x_1 , x_2 and x_3 correspond to x , y and z , respectively. Note that this entire process of computing the effective strains is identical to using the shape function $[N]$ and the strain-displacement matrix $[B]$ for an 8-node brick finite element

$$\{\epsilon\} = [B]\{d\} \quad (3)$$

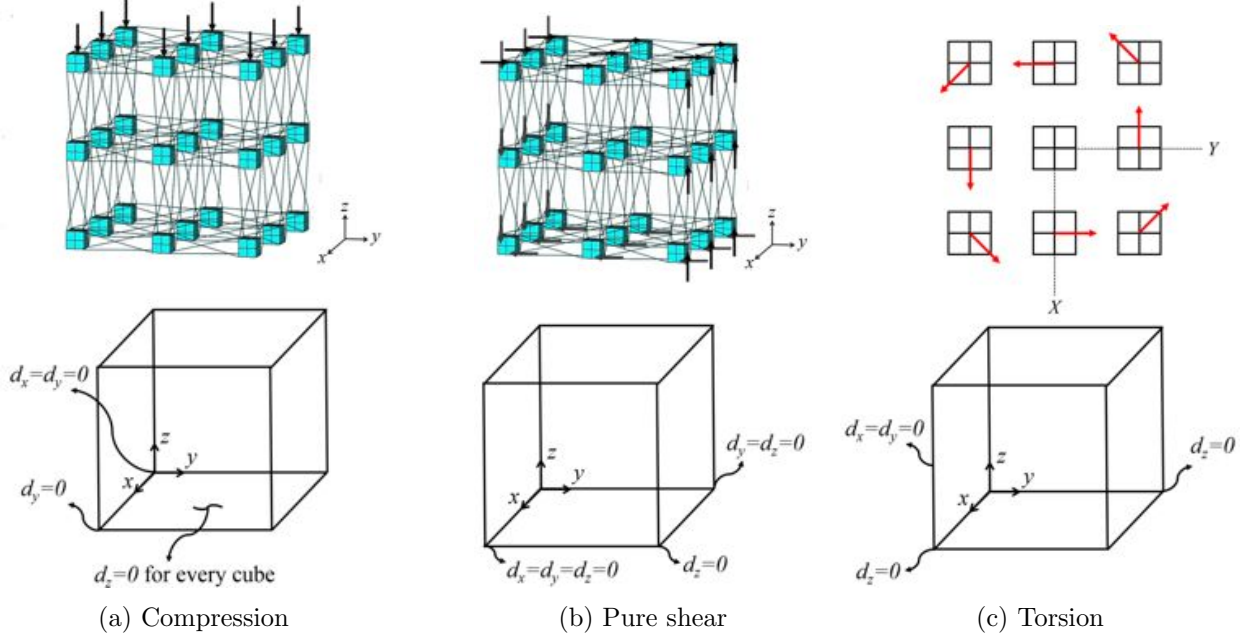


Figure 3: Loading cases for (a) compression, (b) pure shear, and (c) torsion, illustrated for $2 \times 2 \times 2$ lattices. Support conditions (i.e., displacement constraints) are also shown. For (a) and (b), the arrows represent equal point loads. For (c), a local X and Y coordinate system is defined on the upper surface (i.e., the surface with positive z as the normal direction) with origin at the center of this surface, where these directions are parallel to the x and y global coordinate directions of the model. The arrows shown in (c) represent prescribed displacements in the x and y directions as given by equation 11.

where $[B] = [\partial][N]$. Thus, the effective strains throughout each unit cell were determined by evaluating equation 3 with the $[B]$ matrix provided in [27] along with the displacements of each cube in the unit cell obtained from finite element the simulations.

For the three loading cases shown in figure 3, the effective strains of each unit cell were averaged throughout the lattice, which gives rise to bulk effective strains of the lattice $\epsilon_{lattice}$ in a view of continuum. With this, one can determine mechanical properties of the lattice as follow. The effective Young's modulus of the lattice is given by

$$E_z = \frac{\sum_{i=1}^{(n+1)^2} P_i}{A_{eff} \epsilon_{lattice,z}} \quad (4)$$

where P_i represents an applied point load, n is the number of cells per side and A_{eff} is an effective area of the lattice which is defined as $(nL)^2$. Poisson's ratios for two orthogonal directions are determined as

$$\begin{aligned} \nu_{zx} &= -\frac{\epsilon_{lattice,x}}{\epsilon_{lattice,z}} \\ \nu_{zy} &= -\frac{\epsilon_{lattice,y}}{\epsilon_{lattice,z}} \end{aligned} \quad (5)$$

Finally, the effective shear modulus is found as

$$G_{yz} = \frac{\tau}{\gamma_{lattice,yz}} \quad (6)$$

where

$$\tau = \frac{\sum_{i=1}^{(n+1)^2} P_i}{A_{eff}} \quad (7)$$

When the size scale of specimens does not greatly exceed the microstructure size, classical elasticity may not apply. A generalized continuum theory such as Cosserat elasticity is more appropriate; the theory contains characteristic length scales. Cosserat theory of elasticity [28] [29], also known as micropolar elasticity [22], integrates a local rotation of points with respect to each other in addition to the usual translations assumed in classical elasticity.

The stress σ_{jk} (force per unit area) can be asymmetric. The resulting moment is balanced by a couple stress m_{jk} (a torque per unit area). The antisymmetric part of the stress is related to rotations. $\sigma_{jk}^{antisym} = \kappa e_{jkm}(r_m - \phi_m)$ in which κ is an elastic constant, ϕ_m is the rotation of points, called micro-rotation, e_{jkm} is the permutation symbol, and $r_k = \frac{1}{2}e_{klm}u_{m,l}$ is “macro” rotation based on the antisymmetric part of the gradient of displacement u_i . The constitutive equations [22] for linear isotropic Cosserat elasticity are

$$\sigma_{ij} = 2G\epsilon_{ij} + \lambda\epsilon_{kk}\delta_{ij} + \kappa e_{ijk}(r_k - \phi_k) \quad (8)$$

$$m_{ij} = \alpha\phi_{k,k}\delta_{ij} + \beta\phi_{i,j} + \gamma\phi_{j,i} \quad (9)$$

where δ_{ij} is the Kronecker delta and ϵ_{ij} is the microstrain tensor. In three dimensions, the quantities $\lambda, G, \alpha, \beta, \gamma, \kappa$ are six independent Cosserat elastic constants. An isotropic Cosserat solid thus has six elastic constants, whereas a classical elastic solid has two. If $\alpha, \beta, \gamma,$ and κ become zero, the equations of classical elasticity are recovered. The characteristic length in torsion is $\ell_t = \sqrt{\frac{\beta+\gamma}{2G}}$.

Cosserat effects may be revealed via size effects in torsion and in bending. Analytical solutions are available in the literature [30] [31] for round rods of isotropic non-chiral material. There is no known analytical solution for square bars of chiral material. Thus, the solution for an isotropic round bar with chiral material [30], which is exact, is used here

$$G = G_{asy}(1 + 6(\ell_t/r)^2) \left[\frac{1 - 4\Psi\chi/3}{1 - \Psi\chi} \right] \quad (10)$$

where $\chi = I_1(pr)/prI_0(pr)$, $p^2 = 2\kappa/(\alpha + \beta + \gamma)$, and I_0 and I_1 are modified Bessel functions of the first kind. Technical constants include the coupling number which is $N = \sqrt{\frac{\kappa}{2G+\kappa}}$ and the polar ratio is $\Psi = \frac{\beta+\gamma}{\alpha+\beta+\gamma}$. The ratio of Bessel terms inside the square brackets in equation 10 reduces to 1 for $N = 1$.

To study size effects on our lattices, torsion loading was applied by prescribing displacements in the x and y directions (denoted as d_{xi} and d_{yi} , respectively) to each node i at the centers of all cubes on the upper surface of the FEA model (i.e., the surface with positive z as the normal direction, as shown in figure 3c). To determine these displacements, an XY local coordinate system is defined in figure 3c where the X and Y axes are parallel with the x and y axes of a global coordinate system, and the origin of the XY system is at the center of the upper face. The displacements d_{xi} and d_{yi} provide a uniform small rotation η of the upper surface about the $+z$ axis, which is equivalent to applying torque to the lattices in the same direction. The prescribed displacements are determined

as follows. For a particular node i on the upper surface, its position vector, which provides its location relative to the origin of the XY coordinate system, is $\vec{r}_i = X_i \hat{i} + Y_i \hat{j}$, where X_i and Y_i are the coordinates of the node, and \hat{i} and \hat{j} are the usual unit vectors in the x and y directions, respectively. The surface is subjected to a rotation $\vec{\omega} = \eta \hat{k}$ where η is the prescribed small rotation of the surface and \hat{k} is a unit vector in the z direction. Carrying out the cross product $\vec{d}_i = \vec{\omega} \times \vec{r}_i$ provides the prescribed displacements for node i as

$$d_{xi} = -\eta Y_i \quad \text{and} \quad d_{yi} = \eta X_i \quad (11)$$

Rigid body motion of the lattices are suppressed by imposing sufficient boundary constraints on the opposite surface (whose normal is the negative z direction); x and y displacements on one edge were constrained, and the z displacement was constrained at two corner nodes (see figure 3c). Note that all nodes on the upper surface of the FEA model may displace in the z direction, thus the lattices are allowed to freely warp. In order to compute an effective shear modulus $G_{torsion}$ caused by the prescribed displacements, the reaction forces \vec{F}_i for each of the nodes on the upper surface with prescribed displacements was retrieved and a net torque was obtained as

$$\vec{T} = \sum_{i=1}^{(n+1)^2} \vec{r}_i \times \vec{F}_i \quad (12)$$

This torque is in positive z direction and we denote its magnitude by T . The effective shear modulus for all lattice structures with different aspect ratios were then computed as

$$G_{torsion} = \frac{T(nL)}{\eta J} \quad (13)$$

where J is polar moment of inertia which was approximated as $J = \frac{1}{2}\pi(\frac{nL}{2})^4$. The asymptotic shear modulus G_{asy} and the characteristic length ℓ_t were determined by fitting the computed effective shear moduli $G_{torsion}$ of lattice structures (except the 1x1x1 lattice) to equation 10 in nonlinear least-squares sense using MatLab; this fitting also provides p and the coupling number N . Here, the polar ratio Ψ was assumed to be 1.5; size effects are insensitive to Ψ except for size approaching zero. The radius r was taken as half the width of lattices.

Once G_{asy} and ℓ_t were found by fitting computed data to equation 10, the relative stiffness Ω was computed by dividing equation 10 by the asymptotic shear modulus G_{asy} , which gives the size effect as given in equation 14.

$$\Omega = (1 + 6(\ell_t/r)^2) \left[\frac{(1 - 4\Psi\chi/3)}{1 - \Psi\chi} \right] \quad (14)$$

The elastic constants obtained by this process are technical constants not tensorial ones. The reason is that in the absence of an analytical solution for torsion of a chiral square section bar, the solution for a round bar was used. Such a simplification cannot generate size effects via classical elasticity because classical solids do not exhibit size effects, and there is no elastic effect from chirality. The size effects must arise from generalized continuum, e.g. Cosserat, effects in the lattice.

3 Results and discussion

The effective Young's modulus and Poisson's ratio from the compression simulations and the effective shear modulus from the pure shear simulations for all lattice structures (1x1x1 through

6x6x6), and for seven aspect ratios are shown in figures 4, 5 and 6. The objective is to find an aspect ratio that gives rise to elastic isotropy. Note that it was necessary to assume a modulus for rib material in order to determine mechanical properties of the lattices; the modulus of steel was chosen for convenience. Moduli of the lattice depend on the rib material and on geometry. The ratio of the effective Young’s modulus of the lattice to the rib modulus, the relative Young’s modulus, is independent of the assumed rib modulus, as shown in figure 4. Most of the mass in the lattice is in the solid cubical nodules, so the usual modulus versus density plot is not appropriate here. The design is not intended to be light weight; studies of acoustic behavior, which depends on nodule mass, are planned. Poisson’s ratio in two orthogonal directions (i.e., ν_{zx} and ν_{zy}) is found to be identical. As shown in figure 5, when the aspect ratio is about 2, Poisson’s ratio becomes more negative as the number of unit cells per side increases. Moreover, the effective shear modulus varies approximately by a factor of 10^5 .

Note that we have performed a large number of simulations with lattices having different rib slenderness ratios, a/d . As expected, numerical values of the mechanical properties of the lattices depend on this ratio; stiffer lattices can be designed when thicker ribs are used. For example, when the rib slenderness ratio varies from 100 to 5, the magnitude of the effective Young’s modulus of the lattices increases by approximately a factor of 400, and the Poisson effect was reduced by approximately 20 %. However, trends in the mechanical properties of the lattices (e.g., the effective Young’s modulus, Poisson’s ratio and an effective shear modulus) remain the same. Regardless of the rib slenderness ratio, as the number of cells per side increases, a monotonically decreasing trend in the effective Young’s modulus is seen, which tends to converge to a constant value, which is also observed for the effective shear modulus.

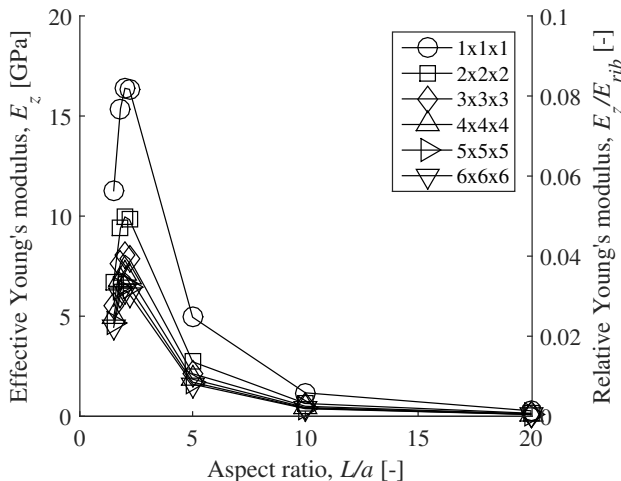


Figure 4: The effective Young’s modulus and the relative Young’s modulus in a principal direction versus aspect ratio.

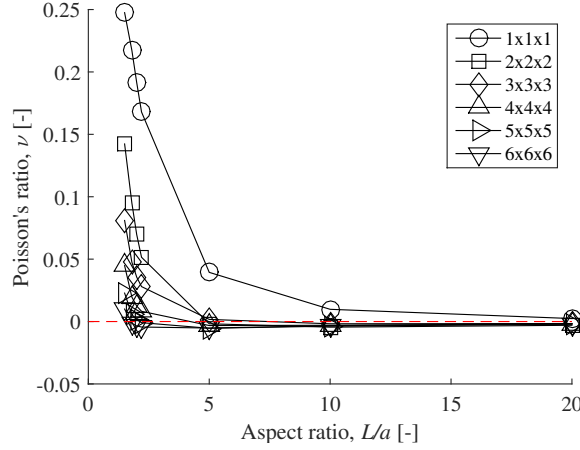


Figure 5: Poisson's ratio in a principal direction versus aspect ratio.

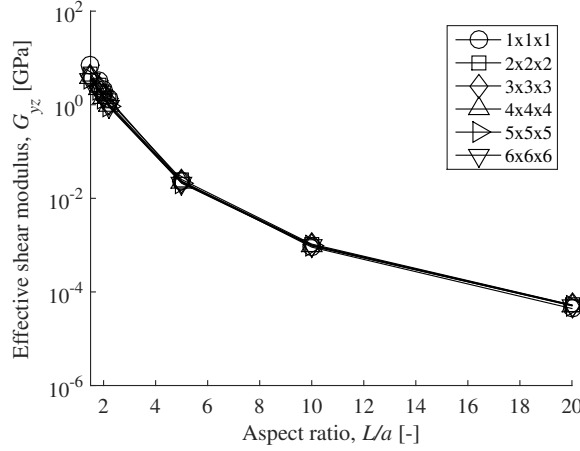


Figure 6: The effective shear modulus (from pure shear) in a principal direction versus aspect ratio.

With computed E_z , ν and G_{yz} above, the measure of isotropy, $E_z/2G_{yz}(1+\nu)$, was determined for all lattice structures except 1x1x1 lattices and for all aspect ratios, as shown in figure 7a. It was found that isotropy occurs when the aspect ratio is between 1.6326 and 1.6466. As seen in figure 7b, the curves for all models are tightly clustered, and the goodness of fit was $R^2 = 1$. Aspect ratio L/a for isotropy was about 1.64, and this is independent of the rib slenderness ratio a/d over a range of values from 100 to 5.

For three dimensional isotropic chiral lattices, the effective Young's modulus in a principal direction versus the number of cells per side is shown in figure 8a. The relative Young's modulus is also plotted in this figure. Note that the aspect ratio of these isotropic lattices was taken as 1.64; this value is an average of computed aspect ratios of all of the lattices that result in isotropy. The Young's modulus monotonically decreases and tends to converge to a constant value as the number of cells increases. A size effect in compression is anticipated in view of the Cosserat continuum in which chiral Cosserat solids have a length scale and coupling between compression and torsion [26], giving rise to stretch-twist coupling, as shown in figure 8d. Poisson's ratio in this continuum view has radial dependence and size effects. A size effect in Poisson's ratio is revealed by FEA. Poisson's

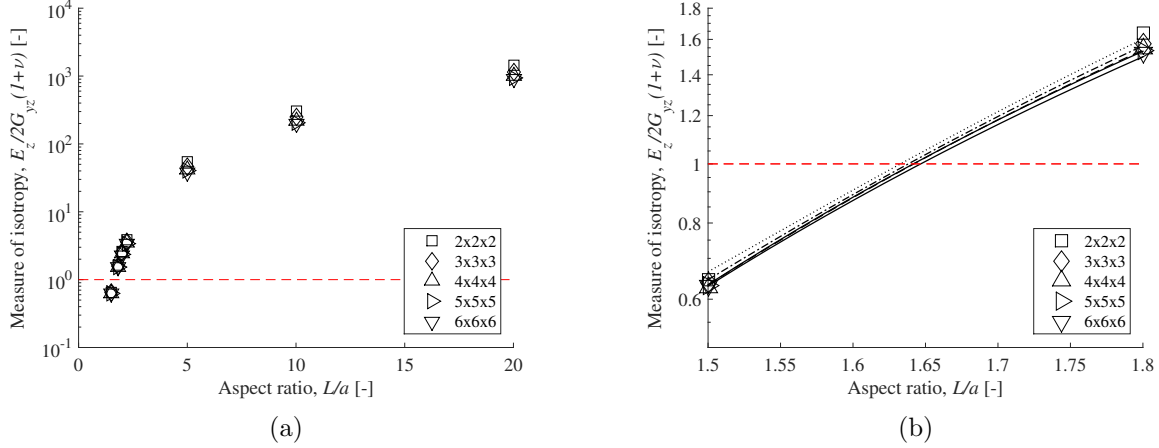


Figure 7: (a) The measure of isotropy vs. the aspect ratio for chiral lattice; a value of 1 indicates elastic isotropy. (b) An expanded scale showing fitting of data points with the least-squares 5th degree polynomial.

ratio is depicted in figure 8b. When $n = 6$, Poisson's ratio becomes almost zero (e.g., $\nu = 0.0024$). Thus, negative Poisson's ratio is expected for a sufficient number of cells. By fitting the computed Poisson's ratio to a power function using nonlinear least-squares, Poisson's ratio becomes negative when n exceeds 7, and its asymptotic value is approximately -0.1393 , as shown in figure 9; the goodness of fit R^2 was 0.99. Note that a slow approach to asymptotic values is anticipated in the Cosserat continuum view. Cosserat elasticity allows the same range of Poisson's ratio [22] as does the classical elasticity. The Cosserat analysis applies to the full range of sizes and Poisson's ratio. Experiments are anticipated for materials with more cells. The effective shear modulus shown in figure 8c has a similar trend compared to the effective Young's modulus.

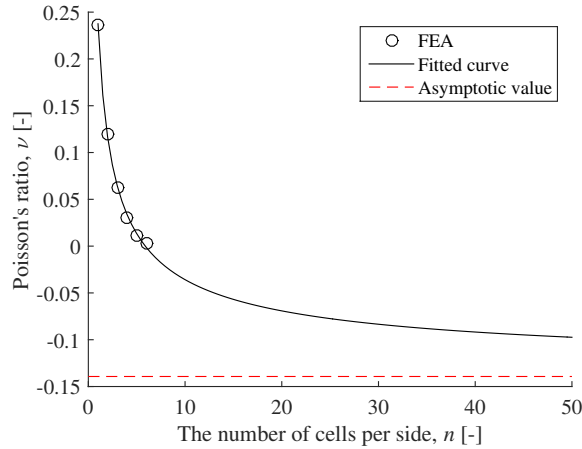


Figure 9: Interpolation and extrapolation of Poisson's ratio to a power function.

Results of torsion size effect studies are depicted in figure 10. For three-dimensional isotropic chiral lattices with a/d equal to 5, $G_{asy} = 0.861$ GPa, $\ell_t = 1.55$ mm, $N = 1$, $\Psi = 1.5$. The goodness of fit was $R^2 = 0.99$. The model with only one cell is excluded for size effect studies, because it is better viewed as a structure. Classical elastic solids, unlike Cosserat solids, have

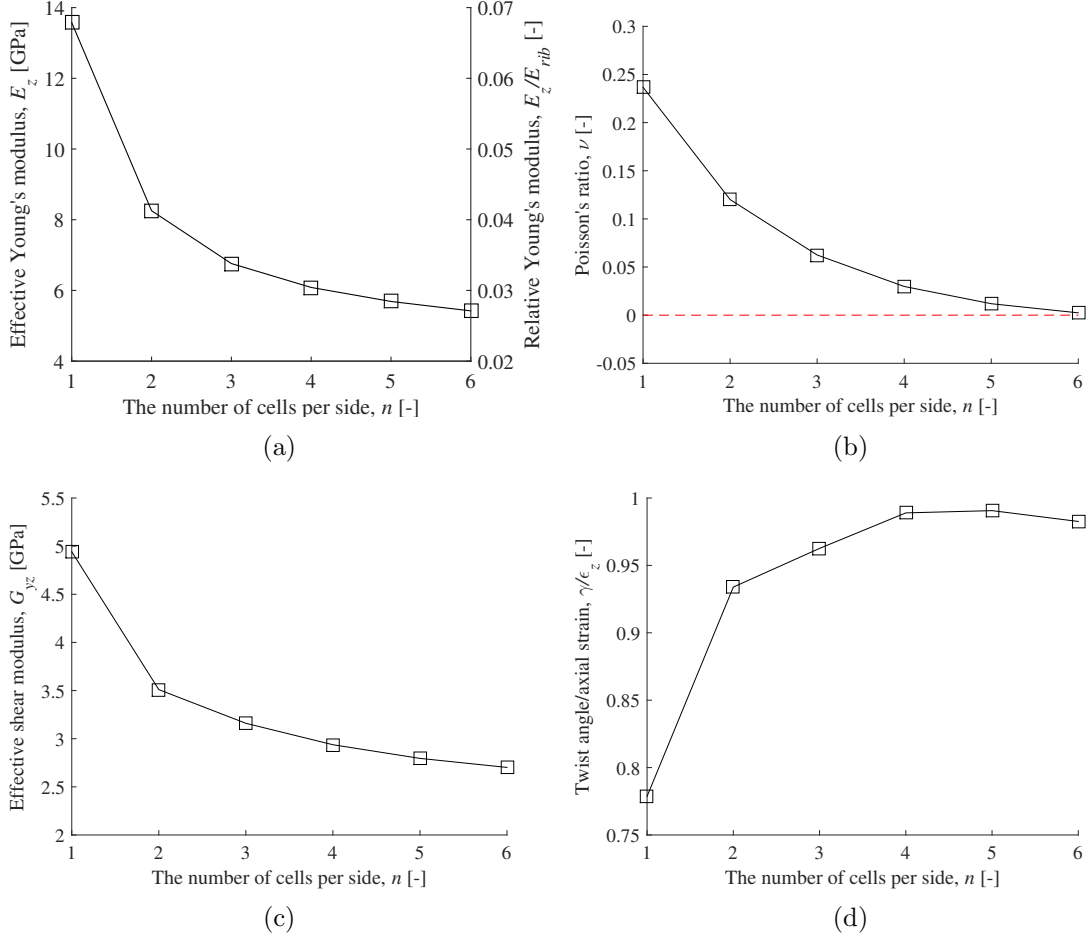


Figure 8: Three dimensional isotropic chiral lattices versus number of cells per side; (a) Effective Young's modulus. (b) Poisson's ratio. (c) Effective shear modulus (d) Stretch-twist coupling.

a relative stiffness equal to 1 independent of size. Lattices presented in this paper clearly show significant size effects. The Cosserat characteristic length ℓ_t is comparable to the nodule spacing $L = 1.64$ mm. Moreover, since N was found to be 1, couple stress theory which is a special case of Cosserat elasticity, is appropriate. Cosserat solids with $N = 1$ (its upper bound) can be interpreted by couple stress theory [32] [34]; this corresponds to $\kappa \rightarrow \infty$; the characteristic length in Cosserat theory is equivalent to $\sqrt{3}$ times the length in couple stress theory. In the present paper, we use symbols after Eringen [22].

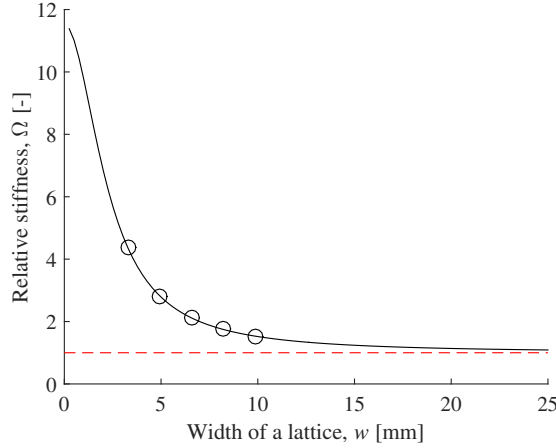


Figure 10: Size effects for three-dimensional isotropic chiral lattices for which $L/a = 1.64$ and nodule spacing $L = 1.64$ mm. Points are obtained via FEA. Curve is theoretical with $G_{asy} = 0.861$ GPa, $\ell_t = 1.55$ mm, $N = 1$, $\Psi = 1.5$; the goodness of fit, $R^2 = 0.99$. Classical elastic solids have $\Omega = 1$ (independent of width).

Size effects can also come from surface effects associated with incomplete cells, surface damage or cell connectivity that ends at the surface; such surface effects produce a softening size effect [35]. These surface effects compete with the stiffening effect of Cosserat elasticity [38]. This is of concern for foams that are cut by a machining process. The softening associated with surface effects can reduce apparent Cosserat parameters but cannot mimic a Cosserat effect because the effect is opposite.

Periodic boundary conditions can simplify analyses in which strain is uniform as in the calculation of Poisson's ratio in hexamer systems [36] [37]; also in analyses of wave motion. Because Cosserat elasticity entails sensitivity to gradients of rotation, and the size effects of interest require a free surface, periodic boundary conditions were not used in the analysis.

The constitutive equations for a Cosserat solid which is isotropic with respect to direction but not with respect to inversions are as follows [26]:

$$\sigma_{kl} = \lambda \epsilon_{rr} \delta_{kl} + 2G \epsilon_{kl} + \kappa e_{klm} (r_m - \phi_m) + C_1 \phi_{r,r} \delta_{kl} + C_2 \phi_{k,l} + C_3 \phi_{l,k} \quad (15)$$

$$m_{kl} = \alpha \phi_{r,r} \delta_{kl} + \beta \phi_{k,l} + \gamma \phi_{l,k} + C_1 \epsilon_{rr} \delta_{kl} + (C_2 + C_3) \epsilon_{kl} + (C_3 - C_2) e_{klm} (r_m - \phi_m) \quad (16)$$

Elastic constants C_1 , C_2 and C_3 are associated with the effect of chirality (i.e., noncentrosymmetry). If these constants vanish, the equations of isotropic micropolar elasticity are recovered. An exact solution for tension / compression of a round chiral Cosserat rod is available [26]; this serves as a guide for the analyst in seeking new effects. There is no available continuum solution for torsion of a square chiral bar, so a finite element approach such as the one used here is appropriate. While it is possible to obtain all six elastic constants of an isotropic Cosserat solid via experiment [39], available analysis does not suffice to determine all nine constants of a chiral solid. Therefore the characteristic length obtained is an effective one.

Chiral lattices may be of interest in the context of the stretch-twist coupling they provide, or for the potential as a framework for isotropic piezoelectric solids [40] which entail Cosserat effects. In such solids, polarization is coupled via an isotropic third rank tensor to the antisymmetric part of the stress.

4 Conclusion

Three dimensional isotropic chiral lattices were developed via finite element analysis. The effective Young's modulus, Poisson's ratio in two orthogonal directions and the effective shear modulus exhibit size effects. Both the effective Young's modulus and the effective shear modulus show convergence to a constant value with an increase of the cells in each side. Poisson's ratio can be negative with sufficient cells. Significant size effects, approaching a factor of five in torsion rigidity, occurred in the lattices. This reveals Cosserat elasticity.

Acknowledgment

Partial support from the NSF via Grant CMMI-1361832 and from the Petroleum Research Fund is gratefully acknowledged.

References

- [1] J. F. Nye, *Physical Properties of Crystals*, Oxford, Clarendon, (1976).
- [2] D. Prall and R. S. Lakes, Properties of a chiral honeycomb with a Poisson's ratio -1, *Int. J. of Mechanical Sciences*, **39**, 305-314, (1996).
- [3] R. S. Lakes, Foam structures with a negative Poisson's ratio, *Science*, **235** 1038-1040 (1987).
- [4] L. J. Gibson, M. F. Ashby, G. S. Schajer, and C. I. Robertson, The mechanics of two dimensional cellular solids, *Proc. Royal Society London*, **A382**, 25-42 (1982).
- [5] A. A. Pozniak and K. W. Wojciechowski, Poisson's ratio of rectangular anti-chiral structures with size dispersion of circular nodes, *Phys. Stat. Sol. (b)* **251**, 367-374, (2014).
- [6] J. Gliick, Anti-rubber, *New York Times* 14 April (1987).
- [7] K. E. Evans, Auxetic polymers - a new range of materials, *Endeavor*, 15 (4), 170-174 (1991).
- [8] K. L. Alderson, A. P. Kettle, K.E. Evans, Novel fabrication route for auxetic polyethylene. Part 1. Processing and microstructure *Polymer Engineering and Science*, 45, 4, 568-578, (2005)
- [9] D. Bornengo, F. Scarpa, C. Remillat, Evaluation of hexagonal chiral structure for morphing airfoil concept, *Proceedings of the Institution of Mechanical Engineers, Part G: Journal of Aerospace Engineering* **219** 185-192 (2005).
- [10] J. Martin, J. Heyder-Bruckner, C. Remillat, F. Scarpa, K. Potter, M. Ruzzene, The hexachiral prismatic wingbox concept, *Phys. Stat. Sol. (b)* **245** 570-571 (2008).
- [11] A. Spadoni, M. Ruzzene and F. Scarpa, Global and local linear buckling behavior of a chiral cellular structure, *Phys. Stat. Sol. (b)* **242** 695-709 (2005).
- [12] W. Miller, C.W. Smith, F. Scarpa, K.E. Evans, Flatwise buckling optimization of hexachiral and tetrachiral honeycombs, *Composites Science and Technology*, **70**, 1049-1056, (2010).
- [13] H. Abramovitch, M. Burgard, L. Edery-Azulay, K.E. Evans, M. Hoffmeister, W. Miller, F. Scarpa, C.W. Smith, K.F. Tee, Smart tetrachiral and hexachiral honeycomb: Sensing and impact detection, *Composites Science and Technology* **70**, 1072-1079 (2010).

- [14] A. Spadoni, M. Ruzzene, S. Gonelli, F. Scarpa, Phononic properties of hexagonal chiral lattices, *Wave Motion* **46** (7), 435-450 (2009).
- [15] L. J. Gibson, and M. F. Ashby, *Cellular Solids*, Pergamon, Oxford, 1988; 2nd Ed., Cambridge, (1997).
- [16] A. J. Jacobsen, W. Barvosa-Carter, S. Nutt, Compression behavior of micro-scale truss structures formed from self-propagating polymer waveguides, *Acta Materialia*, **55**, 6724-6733, (2007).
- [17] A. Alderson, K. E. Evans, Rotation and dilation deformation mechanisms for auxetic behavior in the α -cristobalite tetrahedral framework structure. *Physics and Chemistry of Minerals* **28**(10):711-718 (2001).
- [18] A. Y. Haeri, D. J. Weidner, and J. B. Parise, Elasticity of alpha-cristobalite: a silicon dioxide with a negative Poisson's ratio, *Science*, **257**, 650-652 (1992).
- [19] N. Gaspar, C. W. Smith, A. Alderson, J. N. Grima, K. E. Evans, A generalised three-dimensional tethered-nodule model for auxetic materials. *Journal of Materials Science* **46**(2):372-384 (2011).
- [20] K. L. Alderson, R. S. Webber, K. E. Evans, Microstructural evolution in the processing of auxetic microporous polymers. *Phys Status Solidi B* **244**(3):828-841 (2007).
- [21] T. Buckmann, R. Schittny, M. Thiel, M. Kadic, G. W. Milton and M. Wegener, On three-dimensional dilational elastic metamaterials, *New Journal of Physics* **16** 033032 (2014).
- [22] A.C. Eringen, Theory of micropolar elasticity. In *Fracture Vol. 1*, 621-729 (edited by H. Liebowitz), Academic Press (1968).
- [23] X. N. Liu, G. L. Huang, G. K. Hu, Chiral effect in plane isotropic micropolar elasticity and its application to chiral lattices, *J. of the Mechanics and Physics of Solids* **60**, 1907-1921 (2012).
- [24] A. Spadoni, M. Ruzzene, Elasto-static micropolar behavior of a chiral auxetic lattice, *J. of the Mechanics and Physics of Solids* **60**, 156-171 (2012).
- [25] C. S. Ha, M. E. Plesha, R. S. Lakes, Chiral three dimensional lattices with tunable Poisson's ratio, *Smart Materials and Structures*, accepted, 11.3 (2015).
- [26] R. S. Lakes and R. L. Benedict, Noncentrosymmetry in micropolar elasticity, *International Journal of Engineering Science*, **29** (10), 1161-1167, (1982).
- [27] R. D. Cook, D. S. Malkus, M. E. Plesha, R. J. Witt, *Concepts and Applications of Finite Element Analysis*, 4th edition, John Wiley and Sons publishers, (2002).
- [28] E. Cosserat, and F. Cosserat, *Theorie des Corps Deformables*, Hermann et Fils, Paris (1909).
- [29] R. D. Mindlin, Stress functions for a Cosserat continuum, *Int. J. Solids Structures*, **1**, 265-271 (1965).
- [30] R. D. Gauthier and W. E. Jahsman, A Quest for micropolar elastic constants, *Journal of Applied Mechanics*, **42**(2), 369-374 (1975).

- [31] G. V. Krishna Reddy and N. K. Venkatasubramanian, On the Flexural Rigidity of a Micropolar Elastic Circular Cylinder, *Journal of Applied Mechanics*, **45**(2), 129-431 (1978).
- [32] R. D. Mindlin and H. F. Tiersten, Effect of couple stresses in linear elasticity, *Arch. Rational Mech. Anal.*, **11**, 415-448, (1962)
- [33] S. C. Cowin, Stress functions for Cosserat elasticity, *Int. J. Solids Structures*, **6**, 389-398 (1970)
- [34] S. C. Cowin, An incorrect inequality in micropolar elasticity theory, *J. Appl. Math. Phys. (ZAMP)*, **6**, 389-398 (1970b)
- [35] R. Brezny, and D. J. Green "Characterization of edge effects in cellular materials" *J Materials Sci*, **25**, 4571-4578 (1990).
- [36] K. W. Wojciechowski, 'Constant thermodynamic tension Monte Carlo studies of elastic properties of a two-dimensional systems of hard cyclic hexamers', *Molecular Physics*, **61**, 1247-125 (1987).
- [37] K. W. Wojciechowski, 'Two-dimensional isotropic systems with a negative Poisson ratio', *Physics Letters A137*, 60-64 (1989)
- [38] W. B. Anderson, R. S. Lakes, "Size effects due to Cosserat elasticity and surface damage in closed-cell polymethacrylimide foam", *Journal of Materials Science*, **29**, 6413-6419, (1994).
- [39] R. S. Lakes, Experimental microelasticity of two porous solids, *Int. J. Solids and Structures*, **22** 55-63 (1986).
- [40] R.S. Lakes, Third-rank piezoelectricity in isotropic chiral solids, *Appl. Phys. Lett.*, **106**, 212905, May (2015).